

Dynamics-aware Adversarial Attack of 3D Sparse Convolution Network

An Tao¹ Yueqi Duan¹ He Wang² Ziyi Wu³ Pengliang Ji⁴
 Haowen Sun¹ Jie Zhou¹ Jiwen Lu¹

¹Tsinghua University ²Peking University ³University of Toronto ⁴Beihang University

Abstract

In this paper, we investigate the dynamics-aware adversarial attack problem in deep neural networks. Most existing adversarial attack algorithms are designed under a basic assumption – the network architecture is fixed throughout the attack process. However, this assumption does not hold for many recently proposed networks, e.g. 3D sparse convolution network, which contains input-dependent execution to improve computational efficiency. It results in a serious issue of **lagged gradient**, making the learned attack at the current step ineffective due to the architecture changes afterward. To address this issue, we propose a **Leaded Gradient Method (LGM)** and show the significant effects of the lagged gradient. More specifically, we reformulate the gradients to be aware of the potential dynamic changes of network architectures, so that the learned attack better “leads” the next step than the dynamics-unaware methods when network architecture changes dynamically. Extensive experiments on various datasets show that our LGM achieves impressive performance on semantic segmentation and classification. Compared with the dynamic-unaware methods, LGM achieves about 20% lower mIoU averagely on the ScanNet and S3DIS datasets. LGM also outperforms the recent point cloud attacks.

1. Introduction

As one of the most milestone methods over the past decade in pattern analysis, deep neural networks (DNNs) have greatly improved the performance of many computer vision tasks. In the context of this tremendous success, researchers are surprised to discover that DNNs are vulnerable to adversarial attacks [18, 50], which conceals a great security risk in real-world applications of DNNs. With small but carefully designed perturbations on input examples, attackers can easily force a well-trained model to make mistakes. Various methods are proposed to better attack DNNs to analyze their weakness in different ways and finally improve them [7, 18, 26, 33, 35, 38].

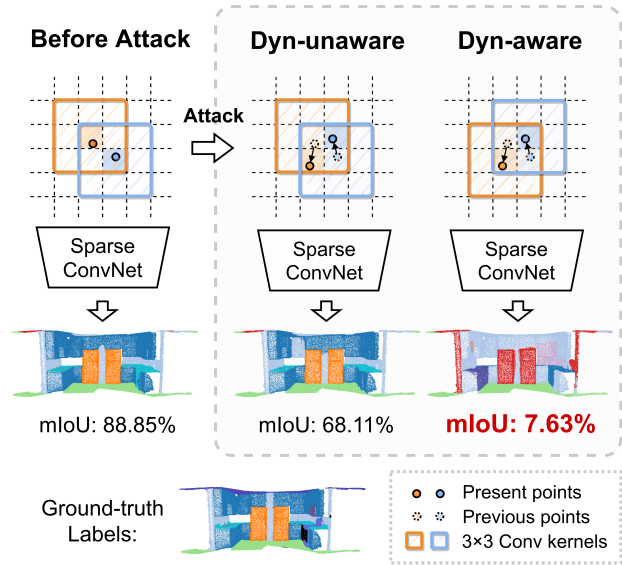


Figure 1. The dynamics-unaware attack directly employs existing traditional methods, which fails to consider the dynamic change of the positions of convolution kernels after attack in sparse convolution network. Instead, our dynamics-aware attack achieves remarkably lower mIoU on the presented point cloud scene. The point perturbation attack in this real-scale scene is restricted to maximum magnitude $\epsilon = 0.01$ m (1 cm). In the figure, “Dyn” is “Dynamics” for short.

Most existing adversarial attack methods assume that the network architecture is fixed throughout the attack process, which is important to guarantee the effectiveness of the attack. At each step, the learned adversarial perturbations targeting the current network are effective since the goal of the attack keeps unchanged. However, this assumption does not hold if the network contains input-dependent execution to improve computational efficiency, such as conditional computation [5, 44], Dynamic DNNs (D²NN) [31], and 3D sparse convolution [10, 19]. When we learn adversarial perturbations at one step, the network architecture changes after we add the perturbations to the input, so that the attack may not be effective due to the change of the

target network. We summarize this issue as **lagged gradient** – we cannot foresee the changed network architecture to back-propagate the true attack gradients at the previous step.

In this paper, we take 3D sparse convolution network as a typical example to study the issue of lagged gradient, which fully exploits the sparsity nature of 3D point cloud data in its architecture and has become a main network type for large-scale 3D scene analysis in self-driving cars and indoor robots [9,22,24,68]. Other than many point-based networks directly take 3D point cloud data as input [32,39,41,55], 3D sparse convolution network first converts point clouds into a number of voxels in the 3D grid with point occupancy, which are called sparse voxels. To keep the sparsity throughout the network, the center of each sparse convolution kernel specifically matches a unique sparse voxel. Therefore, the network architecture of 3D sparse convolution network depends on locations of input voxels, resulting in the attack learned at time t may not be effective due to the dynamic changes of network architecture at time $t + 1$.

To address this issue, we propose a Leaded Gradient Method (LGM) for dynamics-aware adversarial attack of 3D sparse convolution network. We first model the sparse convolution operation into a general form of conventional convolution, where we bring in occupancy values as the mask to represent the centers of the convolution kernels. In this way, although the results of the convolutions centered in unoccupied voxels still keep zero due to the mask, they are enabled to receive non-zero gradients from the attack. As we only operate on a few neighboring unoccupied voxels that may become occupied after one attack step, the extra computational costs are not heavy. Then, we reformulate the gradient that also includes the changes of the occupancy values caused by input perturbations, so that the learned attack is dynamics-aware as the occupancy values can be considered as hyper-parameters of the sparse convolution network. Finally, we carefully design differentiable algorithms to approximate the non-differentiable operations in sparse convolution networks, where we can learn the attack in an end-to-end manner. Figure 1 shows that our dynamics-aware attack significantly outperforms its corresponding dynamics-unaware version as it considers the potential changes of the network architecture.

We conduct extensive adversarial attack experiments on various 3D datasets, including ScanNet [11], S3DIS [1, 2], SemanticKITTI [4], and ModelNet40 [59], for semantic segmentation and classification tasks. In all the datasets, our dynamics-aware attack achieves impressive attack performance, and also significantly outperforms the baseline dynamics-unaware method. On the ScanNet and S3DIS datasets, our LGM achieves about an averagely 20% more drop in mIoU than dynamics-unaware methods. LGM also outperforms the recent point cloud perturbation attacks.

2. Related Work

Adversarial attack. Adversarial examples for deep neural networks are first discovered by Szegedy *et al.* [50]. Goodfellow *et al.* [18] then proposed a Fast Gradient Sign Method (FGSM) to directly generate adversarial examples by adding the clean example with an imperceptibly small vector whose elements are equal to the sign of the elements of the back-propagated gradient of the cost function with respect to the input. On the base of FGSM, Iterative FGSM (I-FGSM) [26], DeepFool [35], and Projected Gradient Descent (PGD) [33] are three representative extensions. Apart from the gradient descent methods, other effective attacks include box-constrained L-BFGS [50], Jacobian-based Saliency Map Attack (JSMA) [38], and the Carlini-Wagner attack (C&W) [7]. The above methods are white-box attacks, where the attacker knows the architecture and weight of the victim models. Considering the details of the models are not usually accessible to attackers, black-box attacks study a situation in which the attacker has no knowledge of the model architecture or weight. These attacks are mainly based on querying the network output logits/probability vectors [8, 20, 49] or output hard labels [6, 13, 14, 36, 37, 62]. Most existing adversarial attacks are based on a fixed network architecture throughout the attack procedure, to our best knowledge, very few works study attacks on networks with dynamic architecture.

3D deep learning. With the proliferation of portable and low-cost LIDAR/RGB-D sensors, an immense amount of 3D data is being collected and therefore requires full utilization. Deep learning has greatly promoted the development of 3D vision understanding in recent years. PointNet [39] and PointNet++ [41] are two pioneer works that exploit deep 3D point cloud processing. Many deep learning architectures on point cloud data are further proposed [12, 28, 32, 51, 55, 57, 64]. In addition to the above method for point cloud, there are many works that focus on other 3D data forms, including voxel [27, 34, 40, 54, 59], mesh [23, 43], multi-view [40, 48], and implicit function [15]. In this paper, we study 3D sparse convolution network, which is first proposed in SSCN [19] for 3D semantic segmentation. The sparsity nature throughout the network makes it naturally suitable for large-scale 3D scene analysis. Many works on sparse convolution network are subsequently proposed for semantic segmentation [9, 10, 68], instance segmentation [16, 22, 24, 25] and object detection [45–47, 63] in various indoor and outdoor scene datasets and achieve state-of-the-art performance. Some works also focus on 3D data attacks. Xiang *et al.* [60] first propose two types of adversarial attacks on point clouds: adversarial point perturbation and adversarial point generation. Recently, many 3D attacks are proposed [21, 29, 30, 52, 53, 56, 61, 65–67]. However, to our best knowledge, very few works study adversarial attack on 3D sparse convolution network.

3. Approach

3.1. Preliminary

Given a point cloud with N points, we define the set of point cloud XYZ coordinates $\mathcal{X}^{\text{pt}} = \{\mathbf{x}_1^{\text{pt}}, \mathbf{x}_2^{\text{pt}}, \dots, \mathbf{x}_N^{\text{pt}}\} \in \mathbb{R}^{N \times 3}$ and features $\mathcal{F}^{\text{pt}} = \{\mathbf{f}_1^{\text{pt}}, \mathbf{f}_2^{\text{pt}}, \dots, \mathbf{f}_N^{\text{pt}}\} \in \mathbb{R}^{N \times D}$. We let $D = 3$ if the features are RGB colors. The set of ground-truth labels $\mathcal{Y}^{\text{pt}} = \{\mathbf{y}_1^{\text{pt}}, \mathbf{y}_2^{\text{pt}}, \dots, \mathbf{y}_N^{\text{pt}}\} \in \{0, 1\}^{N \times Q}$ is constructed by one-hot vectors in Q classes.

After voxelization in 3D grid, N points are converted into M sparse voxels, where $M \leq N$. Each sparse voxel contains at least one point in the point cloud. Following the definitions above, we consider the set of normalized voxel XYZ coordinates $\mathcal{X} = \{\mathbf{x}_1, \mathbf{x}_2, \dots, \mathbf{x}_M\} \in \mathbb{Z}^{M \times 3}$, features $\mathcal{F} = \{\mathbf{f}_1, \mathbf{f}_2, \dots, \mathbf{f}_M\} \in \mathbb{R}^{M \times D}$, and ground-truth labels $\mathcal{Y} = \{\mathbf{y}_1, \mathbf{y}_2, \dots, \mathbf{y}_M\} \in \{0, 1\}^{M \times Q}$. The voxel size is unified as 1 in \mathcal{X} after voxelization.

The sparse convolution network can be defined as:

$$\{\hat{\mathbf{y}}_m\}_{m=1}^M = \text{SCN}(\{(\mathbf{x}_m, \mathbf{f}_m)\}_{m=1}^M, \boldsymbol{\theta}), \quad (1)$$

where $\{\hat{\mathbf{y}}_m\}_{m=1}^M \in \mathbb{R}^{M \times Q}$ is the network output scores for M voxels in Q classes, and $\boldsymbol{\theta}$ represents the network parameters.

3.2. Dynamics-aware Adversarial Attack

In this paper, we focus on white-box attacks using back-propagated gradients throughout the victim network based on the fast gradient method [18, 26]. To illustrate the difference between our dynamics-aware attack and traditional attack, i.e. dynamics-unaware attack, we consider a sparse convolution kernel with weights $\mathbf{W} \in \mathbb{R}^{C \times D' \times D}$ that operates on a voxel coordinate $\mathbf{x}_m \in \mathcal{X}$. The weights \mathbf{W} can be broken done into spatial weights $W_{\mathbf{u}}$ with C matrices of size $D' \times D$, where $\mathbf{u} \in \mathbb{Z}^3$ is a coordinate offset belonging to $\mathcal{S} \in \mathbb{Z}^{C \times 3}$. The convolution output feature $\mathbf{f}'_m \in \mathbb{R}^{D'}$ is derived as:

$$\mathbf{f}'_m = \sum_{\mathbf{x}_q \in \mathcal{K}(\mathbf{x}_m, \mathcal{X}, \mathcal{S})} W_{\mathbf{x}_q - \mathbf{x}_m} \mathbf{f}_q \text{ for } \mathbf{x}_m \in \mathcal{X}, \quad (2)$$

where $\mathcal{K}(\mathbf{x}_m, \mathcal{X}, \mathcal{S}) = \{\mathbf{x}_q | \mathbf{x}_q = \mathbf{x}_m + \mathbf{u} \in \mathcal{X}, \mathbf{x}_q \in \mathcal{X}, \mathbf{u} \in \mathcal{S}\}$ is a collection of sparse voxel coordinates in \mathcal{X} that covered by the kernel shape centered at \mathbf{x}_m . Because in most cases the sparse convolution has no bias, we only show the weights in (2).

However, the sparse convolution only conducts on existence voxel. If the voxel \mathbf{x}_m does not contain point(s) and disappears after one attack step, the convolution on voxel \mathbf{x}_m becomes invalid. This change in network architecture causes the learned perturbation may not be efficient to the changed new architecture. To show this specific characteristic of sparse convolution, we introduce an occupancy function $o(\mathbf{x}, \mathcal{X})$ to indicate the existence of an arbitrary voxel

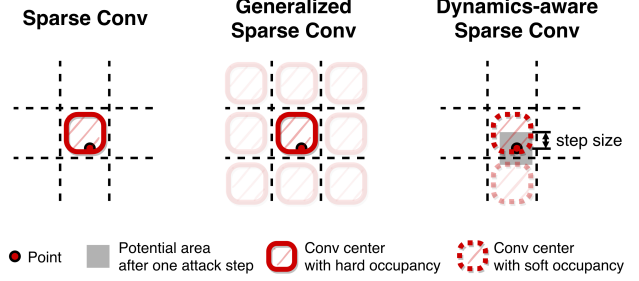


Figure 2. An illustration of sparse convolution in (2), generalized sparse convolution in (4), and our dynamics-aware sparse convolution in (6) with soft occupancy in (10). We only draw the convolution center in this figure for concise, and the color shade indicates the magnitude of the convolution’s occupancy value.

coordinate $\mathbf{x} \in \mathbb{Z}^3$ in current sparse voxels \mathcal{X} :

$$o(\mathbf{x}, \mathcal{X}) = \begin{cases} 1, & \mathbf{x} \in \mathcal{X} \\ 0, & \mathbf{x} \notin \mathcal{X}. \end{cases} \quad (3)$$

Fast gradient method (FGM). In traditional gradient calculation, we actually treat $o(\mathbf{x}, \mathcal{X})$ as a constant value $o_{\mathbf{x}}$. We can release sparse convolution into generalized sparse convolution that operates on every voxels in 3D grid regardless of whether the voxel contains point(s). The two kinds of convolutions share the same weights, and they behave the same when the voxel is valid, i.e. $o_{\mathbf{x}} = 1$. In this case, (2) becomes:

$$\mathbf{f}'_{\text{FGM}} = o_{\mathbf{x}} \left(\sum_{\mathbf{x}_q \in \mathcal{K}(\mathbf{x}, \mathcal{X}, \mathcal{S})} W_{\mathbf{x}_q - \mathbf{x}} \mathbf{f}_q \right) \text{ for } \mathbf{x} \in \mathbb{Z}^3. \quad (4)$$

If the convolution has a bias, the occupancy value is multiplied by the final result of the convolution.

When calculating gradients of an existence voxel \mathbf{x} without consideration of the potential changes of sparse convolution, the partial derivative of \mathbf{f}'_{FGM} with respect to \mathbf{x} is:

$$\frac{\partial \mathbf{f}'_{\text{FGM}}}{\partial \mathbf{x}} = o_{\mathbf{x}} \left(\sum_{\mathbf{x}_q \in \mathcal{K}(\mathbf{x}, \mathcal{X}, \mathcal{S})} W_{\mathbf{x}_q - \mathbf{x}} \frac{\partial \mathbf{f}_q}{\partial \mathbf{x}} \right). \quad (5)$$

Leaded gradient method (LGM). To be aware of the dynamic location of sparse convolution, we consider the changes of the occupancy values $o(\mathbf{x}, \mathcal{X})$ along with the perturbations on the input. We present a dynamics-aware sparse convolution and rewrite (4) as:

$$\mathbf{f}'_{\text{LGM}} = o(\mathbf{x}, \mathcal{X}) \left(\sum_{\mathbf{x}_q \in \mathcal{K}(\mathbf{x}, \mathcal{X}, \mathcal{S})} W_{\mathbf{x}_q - \mathbf{x}} \mathbf{f}_q \right) \text{ for } \mathbf{x} \in \mathbb{Z}^3. \quad (6)$$

Although f'_{FGM} and f'_{LGM} in (4) and (6) are the same in value, the formulas of gradient calculation are different. The partial derivative of f'_{LGM} in (6) with respect to \mathbf{x} is:

$$\begin{aligned} \frac{\partial f'_{\text{LGM}}}{\partial \mathbf{x}} = & o_{\mathbf{x}} \left(\sum_{\mathbf{x}_q \in \mathcal{K}(\mathbf{x}, \mathcal{X}, \mathcal{S})} W_{\mathbf{x}_q - \mathbf{x}} \frac{\partial \mathbf{f}_q}{\partial \mathbf{x}} \right) \\ & + \frac{\partial o(\mathbf{x}, \mathcal{X})}{\partial \mathbf{x}} \left(\sum_{\mathbf{x}_q \in \mathcal{K}(\mathbf{x}, \mathcal{X}, \mathcal{S})} W_{\mathbf{x}_q - \mathbf{x}} \mathbf{f}_q \right). \end{aligned} \quad (7)$$

Compared with traditional fast gradient calculation that does not consider dynamic architecture changes in (5), we can discover that (7) has one more derivative on $\frac{\partial o(\mathbf{x}, \mathcal{X})}{\partial \mathbf{x}}$, which ensures the existence change of convolution is reflected in the back-propagated gradients. Later we will show the hard occupancy $o(\mathbf{x}, \mathcal{X})$ is released into a soft occupancy $\hat{o}(\mathbf{x}, \mathcal{X}^{\text{pt}})$ for our dynamics-aware sparse convolution. The definition domain of \mathbf{x} in (6) is further restricted to existing sparse voxels and a number of surrounding empty voxels for computational cost reduction. Figure 2 illustrates the difference among sparse convolution, generalized sparse convolution and our dynamics-aware sparse convolution in 2D grid.

Non-differentiable function $o(\mathbf{x}, \mathcal{X})$. The occupancy function $o(\mathbf{x}, \mathcal{X})$ is built on the voxel coordinate, while the final goal of our attack is to obtain gradients of input point cloud coordinates \mathcal{X}^{pt} . A straightforward strategy is to further calculate a partial derivative with respect to a point $\mathbf{x}_n^{\text{pt}} \in \mathcal{X}^{\text{pt}}$ as $\frac{\partial \mathbf{x}}{\partial \mathbf{x}_n^{\text{pt}}}$. Because the occupancy function in (3) and the voxelization process are both not everywhere differentiable in the domain of definition, the gradient quality would be poor.

We choose to reformulate the hard occupancy $o(\mathbf{x}, \mathcal{X})$ into a differentiable soft occupancy $\hat{o}(\mathbf{x}, \mathcal{X}^{\text{pt}}) \approx o(\mathbf{x}, \mathcal{X})$ that requires point coordinates as input. We consider the occupancy value of an arbitrary voxel \mathbf{x} in 3D space is essentially determined by a conditional statement: ‘‘If at least one point in the point cloud belongs to the voxel, then the occupancy value is 1, and otherwise 0.’’ This process can be split into two stages: 1) obtain a relation value equal to 1 or 0 to show the existence of the point \mathbf{x}_n^{pt} in the given voxel \mathbf{x} , and 2) gather all the relation values for the given voxel \mathbf{x} together and find whether 1 exists. If at least one relation value equals 1, then the occupancy value of the given voxel is 1, and otherwise 0. However, both the two stages are not everywhere differentiable, so we need to find functions to approximate them.

For the first stage, we follow the Backward Pass Differentiable Approximation (BPDA) method in [3] to present a differentiable function $r(\mathbf{x}, \mathbf{x}_n^{\text{pt}}) \in (0, 1)$ for occupancy calculation. When the point \mathbf{x}_n^{pt} is nearer to the center of the voxel \mathbf{x} , we let the output relation value higher and closer to 1. Some functions have been proposed to solve

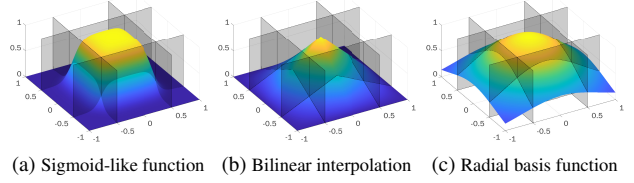


Figure 3. The visualization results on 2D grid for the sigmoid-like function in (9) with $\lambda = 20$, bilinear interpolation [53], and radial basis function [42]. The gray planes show the voxel boundaries. The sigmoid-like function well approximates the original function and has nice gradient quality near the voxel boundaries.

the non-differentiable problem in voxel occupancy, like bilinear interpolation [53] and radial basis function [42]. In this paper, we construct a sigmoid-like function and find it more suitable in attacks of 3D voxel-based network. The differentiable relation function is as follows:

$$\begin{aligned} d(\mathbf{x}, \mathbf{x}_n^{\text{pt}}) &= |(\mathbf{x} + 0.5) - \mathbf{x}_n^{\text{pt}}/L| \quad (8) \\ r(\mathbf{x}, \mathbf{x}_n^{\text{pt}}) &= \prod_{i \in \{0,1,2\}} \frac{1}{1 + \exp(\lambda(d(\mathbf{x}, \mathbf{x}_n^{\text{pt}})[i] - 0.5))}, \quad (9) \end{aligned}$$

where $d(\mathbf{x}, \mathbf{x}_n^{\text{pt}}) \in \mathbb{R}^3$ outputs a distance vector between the point and the voxel center, and L is the voxel size, $d(\mathbf{x}, \mathbf{x}_n^{\text{pt}})[i]$ represents the i -th element in the outputted distance vector of $d(\mathbf{x}, \mathbf{x}_n^{\text{pt}})$, and λ is a parameter that controls the slope near the voxel boundary. Figure 3 shows the visualization results of our sigmoid-like function, bilinear interpolation, and radial basis function. Our sigmoid-like function significantly outperforms the other two existing methods. See supplementary for more details.

For the second stage, we consider the gathering as an ‘‘or’’ operation in nature and present a differentiable function $g(\cdot)$ for this operation. Finally, our reformulated $\hat{o}(\mathbf{x}, \mathcal{X}^{\text{pt}})$ is derived as follows:

$$\begin{aligned} \hat{o}(\mathbf{x}, \mathcal{X}^{\text{pt}}) &= g(\{r(\mathbf{x}, \mathbf{x}_n^{\text{pt}}) | \mathbf{x}_n^{\text{pt}} \in \mathcal{N}(\mathbf{x}, \mathcal{X}^{\text{pt}})\}) \\ &= 1 - \prod_{\mathbf{x}_n^{\text{pt}} \in \mathcal{N}(\mathbf{x}, \mathcal{X}^{\text{pt}})} (1 - r(\mathbf{x}, \mathbf{x}_n^{\text{pt}})), \end{aligned} \quad (10)$$

where $\mathcal{N}(\mathbf{x}, \mathcal{X}^{\text{pt}})$ is a subset of point cloud \mathcal{X}^{pt} to reduce the huge computational costs. For a given voxel \mathbf{x} , we only gather the relation values of those points that possibly exist in the voxel after one attack step. If a voxel has no points to gather values, the voxel is ignored throughout the network. Therefore, we actually extend existing M sparse voxels into M' voxels, by adding a number of surrounding empty voxels that are possibly valid after one attack step. In our implementations, the step size at each iteration to perturb the point cloud coordinates is set very small for better optimizing performance. We find $M' \approx 1.5M$, so the computational cost of our extended convolutions is tolerable. By

multiplying the specially designed occupancy function on every convolution, we can obtain a leaded gradient that is aware of the dynamic network architecture.

End-to-end attack. In this part, we construct an end-to-end gradient for the cost function built on network predictions with respect to input point cloud coordinates. Two issues shatter the gradient propagation and also cause the lagged gradient problem.

The first issue is the non-differentiability in the voxelization process, which makes the gradient unable to be back-propagated from input sparse voxel features to point cloud coordinates. In some networks, the point cloud coordinates are incorporated into their corresponding point cloud features. After the voxelization process, a portion of point coordinates still exists in voxel features, which enables gradient back-propagation. However, not all networks satisfy the above setting. To solve this issue, for a given voxel we first adopt the relation values in (9) as weights to interpolate the voxel features with point coordinates. Similar to the location changes of sparse convolutions in the network, the input sparse voxels will also dynamically change during attacks. We then follow the strategy in leaded gradient formulation to extend the M input voxels into M' voxels.

The second issue is how to construct a cost function on the output of the sparse convolution network. An intuitive way is to directly apply a cost function between the network outputs on M occupied voxels with their ground-truth labels, but the ground-truth voxel labels obtained from point cloud labels will change along with the perturbation of input point cloud coordinates. Similar to the process of voxelization, we conduct a symmetrical process as “devoxelization” by interpolating the label scores from M' sparse voxels into N points. See supplementary for more details on voxelization and devoxelization.

We can derive the final version of our modified sparse convolution network as:

$$\{\hat{\mathbf{y}}_m\}_{m=1}^{M'} = \text{NewSCN}(\{(\mathbf{x}_m, \mathbf{f}_m)\}_{m=1}^{M'}, \mathcal{X}^{\text{pt}}, \theta), \quad (11)$$

where $\{\mathbf{f}_m\}_{m=1}^{M'}$ is reformulated to be controlled by input point cloud coordinates through voxelization, and the voxel predictions $\{\hat{\mathbf{y}}_m\}_{m=1}^{M'}$ will be further converted into point cloud predictions $\{\hat{\mathbf{y}}_n^{\text{pt}}\}_{n=1}^N$ by devoxelization. We then conduct a cost function between the point cloud predictions $\{\hat{\mathbf{y}}_n^{\text{pt}}\}_{n=1}^N$ and ground-truth labels $\{\mathbf{y}_n^{\text{pt}}\}_{n=1}^N$. Compared with (1), we extend the number of input and output voxels into M' and add an input \mathcal{X}^{pt} to indicate that the locations of convolutions are controlled by the occupancy function in (10).

4. Experiments

In this section, we evaluate our proposed dynamics-aware attack on two core tasks in 3D point cloud processing: semantic segmentation and classification, and analyze

its performance against baseline dynamics-unaware methods.

4.1. Datasets

We conduct experiments on four datasets, including the ScanNet, S3DIS, SemanticKITTI, and ModelNet40 datasets.

ScanNet [11] is a large-scale indoor 3D dataset containing 1,613 scans acquired in 707 distinct spaces with semantic annotations. For semantic segmentation, 20 semantic classes are used for evaluation. The dataset is split into 1,201 training scans, 312 validation scans, and 100 testing scans. We perturb the point clouds in validation scans to attack the model.

Stanford 3D Indoor Spaces (S3DIS) [1, 2] includes 271 3D indoor scans across six areas originating from three different buildings of mainly educational and office use. All scans are annotated with 13 semantic classes. We conduct attacks on scans in area 5, while the victim model is trained with the other five areas.

SemanticKITTI [4] is a large-scale outdoor driving-scene 3D dataset containing 43,552 densely annotated LiDAR scans belonging to 22 sequences. It is based on the KITTI Vision Odometry Benchmark [17] and collected by Velodyne-HDLE64 LiDAR in Germany. The dataset splits sequences 00~07 and 09~10 as training set, sequence 08 as the validation set, and sequences 11~21 as the test set. The semantic segmentation is evaluated on 19 classes. We use the validation set to attack the model.

ModelNet40 [59] contains 12,311 3D CAD models from 40 common object categories in the world. It splits 9,843 objects for the training set and 2,468 for the testing set. We follow the data preparation proposed by Qi *et al.* [39] to uniformly sample 2,048 points from the surface of each object. For adversarial attack, we perturb point clouds in the testing set.

4.2. Implementation Details

For both semantic segmentation and classification, we compute a cross-entropy loss over ground-truth labels and their corresponding network output scores for gradient back-propagation. In each attack step, we adopt the normalized gradient method in [29] to constrain the perturbation for each point onto the surface of a 3D cube by L_∞ norm. The step size for each attack step is predefined manually. The attack budget ϵ is the maximum magnitude in L_∞ norm between the original input and the adversarial example.

Throughout the experiments, we present two baseline methods including random perturbation and Fast Gradient Method (FGM). FGM directly adopts the formula in Section 3.1 and constructs the cost function between voxel predictions and ground-truth labels. Other attack details

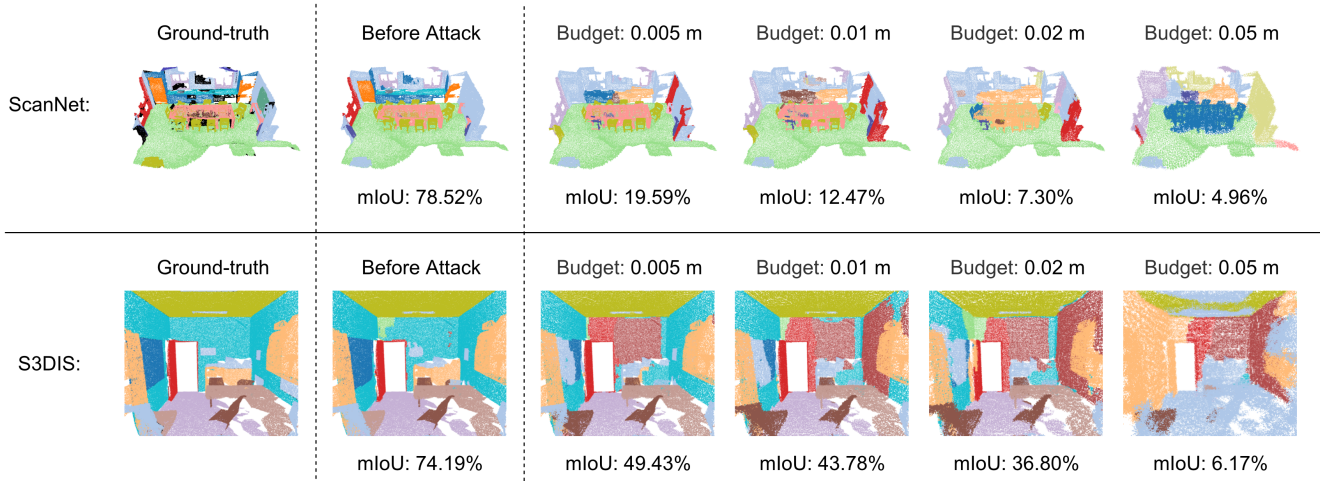


Figure 4. The qualitative visualization results of LGM on the ScanNet validation set and S3DIS area 5 in different budgets (m). The black areas in ground-truth are unlabeled.

of FGM are the same with our Leaded Gradient Method (LGM), including the parameter λ in (9), iteration number, and step size. For a fair comparison, we conduct random perturbation with the same iteration number as FGM and LGM. For some conditions that the point features do not contain point coordinates, i.e., the experiments on the ScanNet and S3DIS datasets, we interpolate the point coordinates into voxel features enable gradient back-propagation.

We also compare our LGM with the recent state-of-the-art methods on adversarial point cloud perturbation. These methods are proposed for single object classification and are based on C&W [7] that requires a distance loss between adversarial sample and its corresponding clean sample. Therefore, they cannot be directly applied to large-scale point cloud scenes for segmentation due to the huge memory costs in distance calculation. Instead, we compare our method with the recent PointPert [60] and KNNPert [52] methods on the object classification task, with implementation codes in [58].

4.3. Results and Analysis

We evaluate the performance of our LGM and other dynamics-unaware methods on two core tasks in 3D point cloud processing: scene-level semantic segmentation and object-level classification.

Scene-level semantic segmentation. Since 3D sparse convolution network is widely used for semantic segmentation in large-scale point cloud scenes, we first present its performance on semantic segmentation under attacks. We adopt MinkowskiNet [10] on the ScanNet, S3DIS, and Cylinder3D [68] on the SemanticKITTI dataset for semantic segmentation. The two network architectures are both built on the base of 3D sparse convolution.

Table 1, 2 and 4 show the attack results on the ScanNet,

Table 1. Point cloud semantic segmentation mIoU results (%) on the ScanNet validation set in different budgets ϵ (m) for various methods.

Method	$\epsilon = 0.005$ m	$\epsilon = 0.01$ m	$\epsilon = 0.02$ m	$\epsilon = 0.05$ m
Bf. Attack	72.22			
Random	71.22	70.07	57.30	15.58
FGM	60.44	55.51	38.65	8.70
LGM	25.79	11.51	5.76	3.83

Table 2. Point cloud semantic segmentation mIoU results (%) on the S3DIS area 5 in different budgets ϵ (m) for various methods.

Method	$\epsilon = 0.005$ m	$\epsilon = 0.01$ m	$\epsilon = 0.02$ m	$\epsilon = 0.05$ m
Bf. Attack	66.35			
Random	61.35	58.50	52.17	23.90
FGM	57.53	52.35	45.24	21.21
LGM	48.20	39.65	30.93	7.45

S3DIS, and SemanticKITTI datasets in different budgets. “Bf. Attack” is “Before Attack” for short. On all datasets with all budgets, our LGM significantly outperforms the dynamics-unaware FGM and random perturbation, which fully validates the importance of the attack method to be aware of the dynamic architecture changes. On the ScanNet and S3DIS datasets, we find the performance drop from FGM to LGM is about twice as much as the drop from random perturbation to FGM. In contrast, the performance drop for LGM on the SemanticKITTI dataset is not as good as the ScanNet and S3DIS datasets. This phenomenon can be explained by the fact that the point cloud coordinates of the SemanticKITTI dataset are included in point features, while the point features of the ScanNet and S3DIS datasets only contain RGB colors. With the included point cloud

Table 3. The class-specific semantic IoUs (%) on the ScanNet validation set in budget $\epsilon = 0.01$ m for various methods.

Method	Wall	Floor	Cab.	Bed	Chair	Sofa	Table	Door	Wind.	Bshf.	Pic.	Cntr.	Desk	Curt.	Fridg.	Shwr.	Toil.	Sink	Bath.	Ofurn.	Mean
Bf. Attack	83.3	94.8	66.0	80.1	91.2	81.7	76.3	61.4	59.1	80.7	29.5	63.3	64.3	75.9	62.1	69.2	92.1	66.8	85.9	60.0	72.2
Random	81.7	94.1	63.5	79.0	90.3	82.5	72.9	56.2	57.0	79.5	26.0	61.4	61.9	73.7	57.2	67.3	91.6	64.6	84.8	56.1	70.1
FGM	70.1	92.6	45.9	73.7	84.0	71.9	55.7	33.5	37.2	58.1	12.5	46.7	37.9	58.0	35.9	47.5	80.6	55.0	77.2	36.4	55.5
LGM	10.8	85.6	5.8	7.7	26.5	10.7	11.8	2.9	2.9	1.1	0.7	0.4	3.6	1.6	0.0	4.0	23.3	7.0	22.7	1.4	11.5

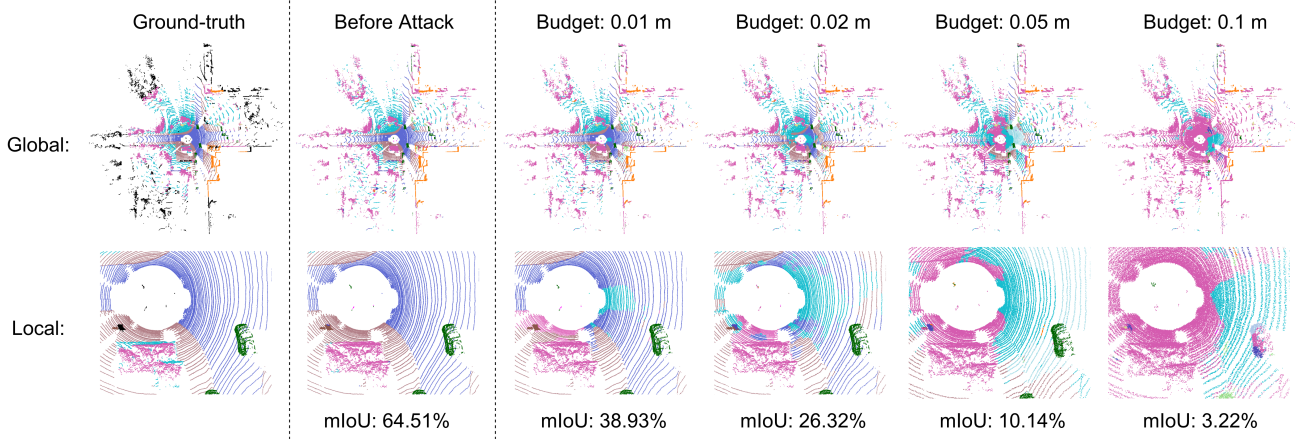


Figure 5. The qualitative visualization results of LGM on the SemanticKITTI validation set in different budgets (m). The scene is presented in both global view and local view. The black areas in ground-truth are ignored labels.

Table 4. Point cloud semantic segmentation mIoU results (%) on the SemanticKITTI validation set in different budgets ϵ (m) for various methods.

Method	$\epsilon = 0.01$ m	$\epsilon = 0.02$ m	$\epsilon = 0.05$ m	$\epsilon = 0.1$ m
Bf. Attack	66.91			
Random	64.71	50.46	18.68	8.74
FGM	36.93	25.61	10.94	5.26
LGM	31.16	19.93	7.28	3.96

coordinates, the gradient back-propagation pass has better quality than those point cloud features that do not include coordinates. Therefore, the impact of dynamic architecture becomes less impressive in the context of a better gradient pass in features.

The results also reveal that there is a distinct performance drop when the budget is close to the voxel size of 0.02 m for the ScanNet dataset and 0.05 m for the S3DIS dataset. When the budget equals the voxel size, all points within a voxel can move out the voxel and their potential destinations cover not only their currently belonged voxel but all surrounding 26 voxels in 3D space. This phenomenon may not be obvious on the SemanticKITTI dataset, since the Cylinder3D network voxelize the point cloud in cylindrical-coordinate system with cylinder partition size $(0.1 \text{ m}, \frac{1}{2\pi}, 0.19 \text{ m})$ for (ρ, θ, z) .

Figure 4 and 5 show the visualization results of our dynamics-aware LGM on the ScanNet, S3DIS, and SemanticKITTI datasets. We observe that the perturbed point cloud coordinates are imperceptible to human eyes in some small budgets, such as budget $\epsilon = 0.005$ m (0.5 cm) and $\epsilon = 0.01$ m (1 cm) on the ScanNet and S3DIS datasets and budget $\epsilon = 0.01$ m (1 cm) and $\epsilon = 0.02$ m (2 cm) on the SemanticKITTI dataset, but these budgets do cause significant wrong predictions of the victim networks. This huge contrast reveals a great security risk in real-world applications of 3D sparse convolution networks.

We also present class-specific semantic IoUs on the ScanNet dataset in Table 3 to show the vulnerability of each class. The results show that other than the class *floor* most classes are easy to attack, which is consistent with the visualization results in Figure 4. The class *wall*, *bed*, *chair*, *toilet* and *bath tub* also have a certain degree of robustness. This may be explained by the fact that these robust classes have discriminative characteristics in their global shapes or locations, therefore they are difficult to be destroyed through local point perturbation by attacks. For the class-specific semantic IoUs on the S3DIS and SemanticKITTI datasets, see supplementary for details.

Object-level classification. We adopt MinkowskiNet [10] on the ModelNet40 dataset for object classification. Table 5 shows the attack results in different bud-

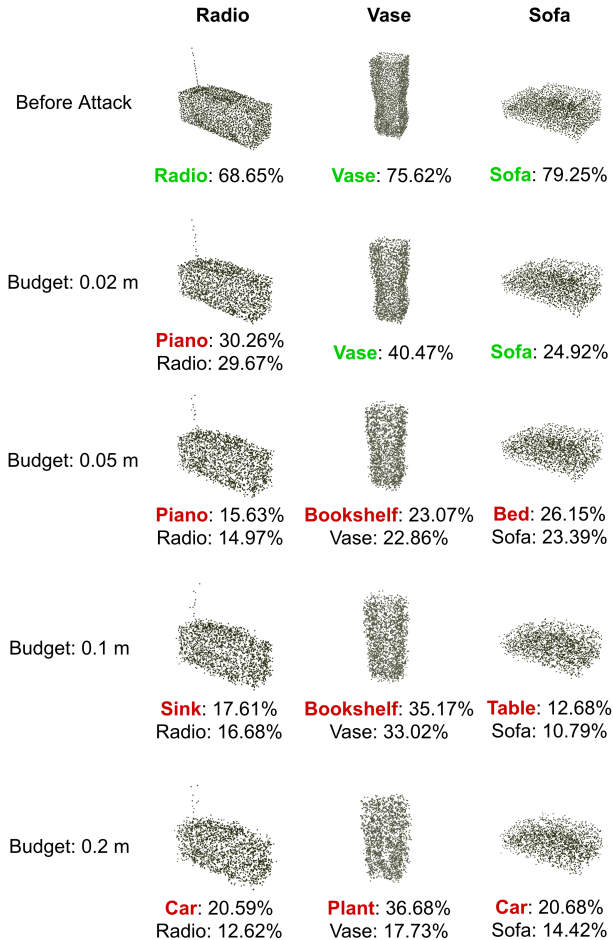


Figure 6. The qualitative visualization results of LGM on the ModelNet40 testing set in different budgets (m).

gets. In all budgets, our LGM outperforms the baseline method FGM and random perturbation, which demonstrates the effectiveness of our dynamics-aware strategy. Since the point cloud features on the ModelNet40 dataset also include point cloud coordinates, the overall performance drop between LGM and FGM compared to the drop between FGM and random perturbation is similar to the SemanticKITTI dataset. We also observe a distinct performance drop when the budget is close to the voxel size 0.05 m (5 cm). Compared with the state-of-the-art point perturbation methods PointPert [60] and KNNPert [52] that do not consider the dynamic network changes of 3D sparse convolution network, our LGM outperforms them in all budgets.

Figure 6 shows the visualization results of our LGM in different budgets. We adopt green color to denote the class prediction is right, and red color to denote the class prediction is wrong. We enclose each prediction with a normalized confidence score output from the network. Because the objects are normalized into a unit sphere in the data preprocessing step, the budget unit may not have any refer-

Table 5. Point cloud classification accuracy results (%) on the ModelNet40 testing set in different budgets ϵ (m) for various methods.

Method	$\epsilon = 0.02$ m	$\epsilon = 0.05$ m	$\epsilon = 0.1$ m	$\epsilon = 0.2$ m
Bf. Attack	92.38			
PointPert [60]	84.40	72.57	35.90	5.51
KNNPert [52]	82.62	59.32	19.81	4.90
Random	85.73	79.09	41.73	6.48
FGM	83.10	64.06	25.85	3.81
LGM	82.46	55.15	19.12	3.12

ence meaning in the real scene. From the visualized objects, we observed that the perturbation is distinct for all budgets. Compared to the attack performance under some imperceptible budgets on the ScanNet, S3DIS, and SemanticKITTI datasets for semantic segmentation, 3D sparse convolution network is relatively more robust to adversarial attack on the ModelNet40 dataset for object classification. From the visualization results, we observe that the wrong prediction of each attacked object does to some extent describe the point cloud shape. Therefore, the attack force the object shape to approach the boundaries between its true class and other classes to fool the victim network. This phenomenon reflects the victim network does learn a certain degree of discriminative information for each class.

5. Conclusion and Discussion

In this paper, we have investigated the lagged gradient issue in adversarial attacks for a kind of network that has dynamic architecture and have proposed a Leaded Gradient Method (LGM) for dynamics-aware adversarial attack. We take 3D sparse convolution network as a typical example to design our method. Specifically, we first analyze the missing part in traditional gradient calculation that considers the architecture changes. We then reformulate the gradient to better “leads” each attack step. Experimental results on semantic segmentation and classification show our LGM achieves impressive performance and outperforms dynamics-unaware baseline methods and recent methods.

Limitations. Our LGM method is based on the conventional FGM method [18, 26] and reformulates the basic gradient to leaded gradient. Further researches can be done on transferring more recent attack methods on top of our leaded gradient to become dynamics-aware.

Negative societal impact. The proposed attack method may cause negative societal impacts in security by generating unnoticeable adversarial examples. This issue warrants further research to deeper investigate attack strategies to better defend them.

References

- [1] Iro Armeni, Sasha Sax, Amir R Zamir, and Silvio Savarese. Joint 2D-3D-semantic data for indoor scene understanding. *arXiv preprint arXiv:1702.01105*, 2017. 2, 5
- [2] Iro Armeni, Ozan Sener, Amir R. Zamir, Helen Jiang, Ioannis Brilakis, Martin Fischer, and Silvio Savarese. 3D semantic parsing of large-scale indoor spaces. In *CVPR*, pages 1534–1543, 2016. 2, 5
- [3] Anish Athalye, Nicholas Carlini, and David Wagner. Obfuscated gradients give a false sense of security: Circumventing defenses to adversarial examples. In *ICML*, pages 274–283, 2018. 4
- [4] Jens Behley, Martin Garbade, Andres Milioto, Jan Quenzel, Sven Behnke, Cyrill Stachniss, and Jurgen Gall. Semantickitti: A dataset for semantic scene understanding of lidar sequences. In *ICCV*, pages 9297–9307, 2019. 2, 5
- [5] Yoshua Bengio, Nicholas Léonard, and Aaron Courville. Estimating or propagating gradients through stochastic neurons for conditional computation. *arXiv preprint arXiv:1308.3432*, 2013. 1
- [6] Wieland Brendel, Jonas Rauber, and Matthias Bethge. Decision-based adversarial attacks: Reliable attacks against black-box machine learning models. In *ICLR*, pages 1–10, 2018. 2
- [7] Nicholas Carlini and David Wagner. Towards evaluating the robustness of neural networks. In *SP*, pages 39–57, 2017. 1, 2, 6
- [8] Pin-Yu Chen, Huan Zhang, Yash Sharma, Jinfeng Yi, and Cho-Jui Hsieh. ZOO: Zeroth order optimization based black-box attacks to deep neural networks without training substitute models. In *ACM AIS workshop*, pages 15–26, 2017. 2
- [9] Ran Cheng, Ryan Razani, Ehsan Taghavi, Enxu Li, and Bingbing Liu. 2-S3Net: Attentive feature fusion with adaptive feature selection for sparse semantic segmentation network. In *CVPR*, pages 12547–12556, 2021. 2
- [10] Christopher Choy, JunYoung Gwak, and Silvio Savarese. 4D spatio-temporal convnets: Minkowski convolutional neural networks. In *CVPR*, pages 3075–3084, 2019. 1, 2, 6, 7
- [11] Angela Dai, Angel X. Chang, Manolis Savva, Maciej Halber, Thomas Funkhouser, and Matthias Nießner. ScanNet: Richly-annotated 3D reconstructions of indoor scenes. In *CVPR*, pages 5828–5839, 2017. 2, 5
- [12] Congyue Deng, Or Litany, Yueqi Duan, Adrien Poulernard, Andrea Tagliasacchi, and Leonidas J. Guibas. Vector neurons: A general framework for SO(3)-equivariant networks. In *ICCV*, pages 12200–12209, 2021. 2
- [13] Yinpeng Dong, Fangzhou Liao, Tianyu Pang, Hang Su, Jun Zhu, Xiaolin Hu, and Jianguo Li. Boosting adversarial attacks with momentum. In *CVPR*, pages 9185–9193, 2018. 2
- [14] Yinpeng Dong, Tianyu Pang, Hang Su, and Jun Zhu. Evading defenses to transferable adversarial examples by translation-invariant attacks. In *CVPR*, pages 4312–4321, 2019. 2
- [15] Yueqi Duan, Haidong Zhu, He Wang, Li Yi, Ram Nevatia, and Leonidas J. Guibas. Curriculum DeepSDF. In *ECCV*, pages 51–67, 2020. 2
- [16] Francis Engelmann, Martin Bokeloh, Alireza Fathi, Bastian Leibe, and Matthias Nießner. 3D-MPA: Multi-proposal aggregation for 3D semantic instance segmentation. In *CVPR*, pages 9031–9040, 2020. 2
- [17] Andreas Geiger, Philip Lenz, and Raquel Urtasun. Are we ready for autonomous driving? the KITTI vision benchmark suite. In *CVPR*, pages 3354–3361, 2012. 5
- [18] Ian J. Goodfellow, Jonathon Shlens, and Christian Szegedy. Explaining and harnessing adversarial examples. In *ICLR*, pages 1–11, 2015. 1, 2, 3, 8
- [19] Benjamin Graham, Martin Engelcke, and Laurens Van Der Maaten. 3D semantic segmentation with submanifold sparse convolutional networks. In *CVPR*, pages 9224–9232, 2018. 1, 2
- [20] Chuan Guo, Jacob Gardner, Yurong You, Andrew Gordon Wilson, and Kilian Weinberger. Simple black-box adversarial attacks. In *ICML*, pages 2484–2493, 2019. 2
- [21] Abdullah Hamdi, Sara Rojas, Ali Thabet, and Bernard Ghanem. AdvPC: Transferable adversarial perturbations on 3D point clouds. In *ECCV*, pages 241–257, 2020. 2
- [22] Lei Han, Tian Zheng, Lan Xu, and Lu Fang. Occuseg: Occupancy-aware 3D instance segmentation. In *CVPR*, pages 2940–2949, 2020. 2
- [23] Rana Hanocka, Amir Hertz, Noa Fish, Raja Giryes, Shachar Fleishman, and Daniel Cohen-Or. MeshCNN: a network with an edge. *TOG*, 38(4):1–12, 2019. 2
- [24] Wenbo Hu, Hengshuang Zhao, Li Jiang, Jiaya Jia, and Tien-Tsin Wong. Bidirectional projection network for cross dimension scene understanding. In *CVPR*, pages 14373–14382, 2021. 2
- [25] Li Jiang, Hengshuang Zhao, Shaoshuai Shi, Shu Liu, Chi-Wing Fu, and Jiaya Jia. PointGroup: Dual-set point grouping for 3D instance segmentation. In *CVPR*, pages 4867–4876, 2020. 2
- [26] Alexey Kurakin, Ian Goodfellow, Samy Bengio, et al. Adversarial examples in the physical world, 2017. 1, 2, 3, 8
- [27] Truc Le and Ye Duan. Pointgrid: A deep network for 3D shape understanding. In *CVPR*, pages 9204–9214, 2018. 2
- [28] Yangyan Li, Rui Bu, Mingchao Sun, Wei Wu, Xinhan Di, and Baoquan Chen. PointCNN: Convolution on X-transformed points. In *NeurIPS*, pages 828–838, 2018. 2
- [29] Daniel Liu, Ronald Yu, and Hao Su. Extending adversarial attacks and defenses to deep 3D point cloud classifiers. In *ICIP*, pages 2279–2283, 2019. 2, 5
- [30] Daniel Liu, Ronald Yu, and Hao Su. Adversarial shape perturbations on 3D point clouds. In *ECCV*, pages 88–104, 2020. 2
- [31] Lanlan Liu and Jia Deng. Dynamic deep neural networks: Optimizing accuracy-efficiency trade-offs by selective execution. In *AAAI*, pages 3675–3682, 2018. 1
- [32] Yongcheng Liu, Bin Fan, Shiming Xiang, and Chunhong Pan. Relation-shape convolutional neural network for point cloud analysis. In *CVPR*, pages 8895–8904, 2019. 2
- [33] Aleksander Madry, Aleksandar Makelov, Ludwig Schmidt, Dimitris Tsipras, and Adrian Vladu. Towards deep learning models resistant to adversarial attacks. In *ICLR*, pages 1–10, 2018. 1, 2

- [34] Daniel Maturana and Sebastian Scherer. Voxnet: A 3D convolutional neural network for real-time object recognition. In *IROS*, pages 922–928, 2015. 2
- [35] Seyed-Mohsen Moosavi-Dezfooli, Alhussein Fawzi, and Pascal Frossard. Deepfool: a simple and accurate method to fool deep neural networks. In *CVPR*, pages 2574–2582, 2016. 1, 2
- [36] Nicolas Papernot, Patrick McDaniel, and Ian Goodfellow. Transferability in machine learning: from phenomena to black-box attacks using adversarial samples. *arXiv preprint arXiv:1605.07277*, 2016. 2
- [37] Nicolas Papernot, Patrick McDaniel, Ian Goodfellow, Somesh Jha, Z Berkay Celik, and Ananthram Swami. Practical black-box attacks against machine learning. In *ACM ACCCS*, pages 506–519, 2017. 2
- [38] Nicolas Papernot, Patrick McDaniel, Somesh Jha, Matt Fredrikson, Z Berkay Celik, and Ananthram Swami. The limitations of deep learning in adversarial settings. In *EuroSP*, pages 372–387, 2016. 1, 2
- [39] Charles R. Qi, Hao Su, Kaichun Mo, and Leonidas J. Guibas. PointNet: Deep learning on point sets for 3D classification and segmentation. In *CVPR*, pages 652–660, 2017. 2, 5
- [40] Charles R. Qi, Hao Su, Matthias Nießner, Angela Dai, Mengyuan Yan, and Leonidas J. Guibas. Volumetric and multi-view CNNs for object classification on 3D data. In *CVPR*, pages 5648–5656, 2016. 2
- [41] Charles R. Qi, Li Yi, Hao Su, and Leonidas J. Guibas. PointNet++: Deep hierarchical feature learning on point sets in a metric space. In *NeurIPS*, pages 5105–5114, 2017. 2
- [42] Rui Qian, Divyansh Garg, Yan Wang, Yurong You, Serge Belongie, Bharath Hariharan, Mark Campbell, Kilian Q Weinberger, and Wei-Lun Chao. End-to-end pseudo-lidar for image-based 3D object detection. In *CVPR*, pages 5881–5890, 2020. 4, 12
- [43] Jonas Schult, Francis Engelmann, Theodora Kontogianni, and Bastian Leibe. DualConvMesh-Net: Joint geodesic and euclidean convolutions on 3D meshes. In *CVPR*, pages 8612–8622, 2020. 2
- [44] Noam Shazeer, Azalia Mirhoseini, Krzysztof Maziarz, Andy Davis, Quoc Le, Geoffrey Hinton, and Jeff Dean. Outrageously large neural networks: The sparsely-gated mixture-of-experts layer. *arXiv preprint arXiv:1701.06538*, 2017. 1
- [45] Shaoshuai Shi, Chaoxu Guo, Li Jiang, Zhe Wang, Jianping Shi, Xiaogang Wang, and Hongsheng Li. PV-RCNN: Point-voxel feature set abstraction for 3D object detection. In *CVPR*, pages 10529–10538, 2020. 2
- [46] Shaoshuai Shi, Li Jiang, Jiajun Deng, Zhe Wang, Chaoxu Guo, Jianping Shi, Xiaogang Wang, and Hongsheng Li. Pvrnn++: Point-voxel feature set abstraction with local vector representation for 3D object detection. *arXiv preprint arXiv:2102.00463*, 2021. 2
- [47] Shaoshuai Shi, Zhe Wang, Jianping Shi, Xiaogang Wang, and Hongsheng Li. From points to parts: 3D object detection from point cloud with part-aware and part-aggregation network. *PAMI*, 2020. 2
- [48] Hang Su, Subhransu Maji, Evangelos Kalogerakis, and Erik Learned-Miller. Multi-view convolutional neural networks for 3D shape recognition. In *ICCV*, pages 945–953, 2015. 2
- [49] Jiawei Su, Danilo Vasconcellos Vargas, and Kouichi Sakurai. One pixel attack for fooling deep neural networks. *EC*, 23(5):828–841, 2019. 2
- [50] Christian Szegedy, Wojciech Zaremba, Ilya Sutskever, Joan Bruna, Dumitru Erhan, Ian Goodfellow, and Rob Fergus. Intriguing properties of neural networks. In *ICLR*, pages 1–10, 2014. 1, 2
- [51] Hugues Thomas, Charles R. Qi, Jean-Emmanuel Deschaud, Beatriz Marcotegui, François Goulette, and Leonidas J. Guibas. KPConv: Flexible and deformable convolution for point clouds. In *ICCV*, pages 6411–6420, 2019. 2
- [52] Tzungyu Tsai, Kaichen Yang, Tsung-Yi Ho, and Yier Jin. Robust adversarial objects against deep learning models. In *AAAI*, pages 954–962, 2020. 2, 6, 8
- [53] James Tu, Mengye Ren, Sivabalan Manivasagam, Ming Liang, Bin Yang, Richard Du, Frank Cheng, and Raquel Urtasun. Physically realizable adversarial examples for lidar object detection. In *CVPR*, pages 13716–13725, 2020. 2, 4, 12
- [54] Peng-Shuai Wang, Yang Liu, Yu-Xiao Guo, Chun-Yu Sun, and Xin Tong. O-CNN: Octree-based convolutional neural networks for 3D shape analysis. *TOG*, 36(4):1–11, 2017. 2
- [55] Yue Wang, Yongbin Sun, Ziwei Liu, Sanjay E. Sarma, Michael M. Bronstein, and Justin M. Solomon. Dynamic graph CNN for learning on point clouds. *TOG*, 38(5):1–12, 2019. 2
- [56] Yuxin Wen, Jiehong Lin, Ke Chen, CL Philip Chen, and Kui Jia. Geometry-aware generation of adversarial point clouds. *PAMI*, 2020. 2
- [57] Wenxuan Wu, Zhongang Qi, and Li Fuxin. PointConv: Deep convolutional networks on 3D point clouds. In *CVPR*, pages 9621–9630, 2019. 2
- [58] Ziyi Wu, Yueqi Duan, He Wang, Qingnan Fan, and Leonidas J Guibas. If-Defense: 3D adversarial point cloud defense via implicit function based restoration. *arXiv preprint arXiv:2010.05272*, 2020. 6
- [59] Zhirong Wu, Shuran Song, Aditya Khosla, Fisher Yu, Linguang Zhang, Xiaoou Tang, and Jianxiong Xiao. 3D shapenets: A deep representation for volumetric shapes. In *CVPR*, pages 1912–1920, 2015. 2, 5
- [60] Chong Xiang, Charles R. Qi, and Bo Li. Generating 3D adversarial point clouds. In *CVPR*, pages 9136–9144, 2019. 2, 6, 8
- [61] Zhen Xiang, David J. Miller, Siheng Chen, Xi Li, and George Kesidis. A backdoor attack against 3D point cloud classifiers. In *ICCV*, pages 7597–7607, 2021. 2
- [62] Cihang Xie, Zhishuai Zhang, Yuyin Zhou, Song Bai, Jianyu Wang, Zhou Ren, and Alan L Yuille. Improving transferability of adversarial examples with input diversity. In *CVPR*, pages 2730–2739, 2019. 2
- [63] Yan Yan, Yuxing Mao, and Bo Li. Second: Sparsely embedded convolutional detection. *Sensors*, 18(10):3337, 2018. 2
- [64] Hengshuang Zhao, Li Jiang, Chi-Wing Fu, and Jiaya Jia. PointWeb: Enhancing local neighborhood features for point cloud processing. In *CVPR*, pages 5565–5573, 2019. 2
- [65] Yue Zhao, Yuwei Wu, Caihua Chen, and Andrew Lim. On isometry robustness of deep 3D point cloud models under adversarial attacks. In *CVPR*, pages 1201–1210, 2020. 2

- [66] Tianhang Zheng, Changyou Chen, Junsong Yuan, Bo Li, and Kui Ren. Pointcloud saliency maps. In *ICCV*, pages 1598–1606, 2019. [2](#)
- [67] Hang Zhou, Dongdong Chen, Jing Liao, Kejiang Chen, Xiaoyi Dong, Kunlin Liu, Weiming Zhang, Gang Hua, and Nenghai Yu. LG-GAN: Label guided adversarial network for flexible targeted attack of point cloud based deep networks. In *CVPR*, pages 10356–10365, 2020. [2](#)
- [68] Xinge Zhu, Hui Zhou, Tai Wang, Fangzhou Hong, Yuexin Ma, Wei Li, Hongsheng Li, and Dahua Lin. Cylindrical and asymmetrical 3D convolution networks for lidar segmentation. In *CVPR*, pages 9939–9948, 2021. [2](#), [6](#)

Appendix

A. Relation Function

In the main text, we present a sigmoid-like function for occupancy calculation. There are two existing functions can also be adopted in this situation, bilinear interpolation [53] and radial basis function [42]. The formula of bilinear interpolation (BI) is as follows:

$$r_{\text{BI}}(\mathbf{x}, \mathbf{x}_n^{\text{pt}}) = \prod_{i \in \{0,1,2\}} (1 - d(\mathbf{x}, \mathbf{x}_n^{\text{pt}})[i]) \quad (12)$$

where $d(\mathbf{x}, \mathbf{x}_n^{\text{pt}})$ is outputs a distance vector between the voxel center \mathbf{x} and the point \mathbf{x}_n^{pt} . The formula of radial basis function (RBF) is as follows:

$$r_{\text{RBF}}(\mathbf{x}, \mathbf{x}_n^{\text{pt}}) = \frac{1}{\alpha} \exp(-\|d(\mathbf{x}, \mathbf{x}_n^{\text{pt}})\|^2) \quad (13)$$

where α is a parameter to control the intensity. When the point \mathbf{x}_n^{pt} belongs to the voxel \mathbf{x} , $\alpha = 1$, and otherwise $\alpha = 26$ (considering 26 neighbors in a $3 \times 3 \times 3$ range).

Compared to bilinear interpolation and radial basis function, our sigmoid-like function has two important qualities: 1) the output of the sigmoid-like function is similar to the original hard function in most areas, so the sigmoid-like function can substitute the original function in forwarding propagation; 2) the sigmoid-like function has significant gradient variation near voxel boundaries. Therefore, when a point locates near the voxel boundary, the gradient will become distinctly large to force the point to quickly move in/out the voxel, instead of staying near the boundary.

Table 6 shows the performance on the ScanNet validation set in different budgets. The results validate the effectiveness of our sigmoid-like function (denoted as Sigmoid).

B. Attack Details

In this section, we give more details of our voxelization and devoxelization process for an end-to-end attack.

Voxelization. we first present the formulas of normal practice for voxel-based networks. Following the definitions in the main text, we denote the set of point cloud XYZ coordinates $\mathcal{X}^{\text{pt}} = \{\mathbf{x}_n^{\text{pt}}\}_{n=1}^N$, features $\mathcal{F}^{\text{pt}} = \{\mathbf{f}_n^{\text{pt}}\}_{n=1}^N$, and ground-truth labels $\mathcal{Y}^{\text{pt}} = \{\mathbf{y}_n^{\text{pt}}\}_{n=1}^N$, and the set of voxel XYZ coordinates $\mathcal{X} = \{\mathbf{x}_m\}_{m=1}^M$, features $\mathcal{F} = \{\mathbf{f}_m\}_{m=1}^M$, and ground-truth labels $\mathcal{Y} = \{\mathbf{y}_m\}_{m=1}^M$. The normal voxelization process can be described as follows:

$$\tilde{\mathbf{x}}_n = \text{Floor}(\mathbf{x}_n^{\text{pt}}/L) \text{ for } \mathbf{x}_n^{\text{pt}} \in \mathcal{X}^{\text{pt}} \quad (14)$$

$$\{\tilde{\mathbf{x}}_n\}_{n \in \mathcal{I}} = \text{Unique}(\{\tilde{\mathbf{x}}_n\}_{n=1}^N) \quad (15)$$

$$\{\mathbf{x}_m\}_{m=1}^M = \{\tilde{\mathbf{x}}_n\}_{n \in \mathcal{I}} \quad (16)$$

$$\{(\mathbf{f}_m, \mathbf{y}_m)\}_{m=1}^M = \{(\mathbf{f}_n^{\text{pt}}, \mathbf{y}_n^{\text{pt}})\}_{n \in \mathcal{I}}, \quad (17)$$

Table 6. Point cloud semantic segmentation mIoU results (%) on the ScanNet validation set in different budgets ϵ (m) for various occupancy functions.

Method	$\epsilon = 0.005$ m	$\epsilon = 0.01$ m	$\epsilon = 0.02$ m	$\epsilon = 0.05$ m
Bf. Attack	72.22			
BI [53]	68.08	60.21	32.62	11.73
RBF [42]	36.14	16.62	8.29	5.00
Sigmoid	25.79	11.51	5.76	3.83

where L is the voxel size, and indices \mathcal{I} is a subset of $\{n\}_{n=1}^N$ that satisfies $|\mathcal{I}| = M$.

Because the normal voxelization process is non-differentiable and dynamics-unaware, we then follow the strategy in leded gradient formulation to use a differentiable function to interpolate the voxel features with point coordinates and extend the M input voxels into M' voxels. We use \mathcal{X}' to denote the M' voxel coordinates with extended voxels. The existences of these M' input voxel features are control by occupancy function. For a voxel $\mathbf{x}_m \in \mathcal{X}'$, the input voxel feature \mathbf{f}_m is derived as:

$$\tilde{\mathbf{f}}_m = \frac{\sum_{\mathbf{x}_n^{\text{pt}} \in \mathcal{N}(\mathbf{x}_m, \mathcal{X}^{\text{pt}})} r(\mathbf{x}_m, \mathbf{x}_n^{\text{pt}}) \mathbf{f}_n^{\text{pt}}}{\sum_{\mathbf{x}_n^{\text{pt}} \in \mathcal{N}(\mathbf{x}_m, \mathcal{X}^{\text{pt}})} r(\mathbf{x}_m, \mathbf{x}_n^{\text{pt}})} \quad (18)$$

$$\mathbf{f}_m = \hat{o}(\mathbf{x}_m, \mathcal{X}^{\text{pt}}) \tilde{\mathbf{f}}_m. \quad (19)$$

where $r(\mathbf{x}_m, \mathbf{x}_n^{\text{pt}})$ and $\hat{o}(\mathbf{x}_m, \mathcal{X}^{\text{pt}})$ are defined in (9) and (10).

Devoxelization. Symmetrical to the voxelization process, we conduct a ‘‘devoxelization’’ process on the network voxel outputs by interpolating the label scores from M' sparse voxels into N points. Because the M' outputs of the network are already multiplied with occupancy values in (2). we first divide the outputs by their occupancy values to recover the natural values. Then, we interpolate the label scores from M' sparse voxels into N points. The label score $\hat{\mathbf{y}}_n^{\text{pt}}$ for point $\mathbf{x}_n^{\text{pt}} \in \mathcal{X}^{\text{pt}}$ is derived as follows:

$$\tilde{\mathbf{y}}_m = \frac{\hat{\mathbf{y}}_m}{\hat{o}(\mathbf{x}_m, \mathcal{X}^{\text{pt}})} \quad (20)$$

$$\hat{\mathbf{y}}_n^{\text{pt}} = \frac{\sum_{\mathbf{x}_m \in \mathcal{M}(\mathbf{x}_n^{\text{pt}}, \mathcal{X}')} r(\mathbf{x}_m, \mathbf{x}_n^{\text{pt}}) \tilde{\mathbf{y}}_m}{\sum_{\mathbf{x}_m \in \mathcal{M}(\mathbf{x}_n^{\text{pt}}, \mathcal{X}')} r(\mathbf{x}_m, \mathbf{x}_n^{\text{pt}})}, \quad (21)$$

where $\hat{\mathbf{y}}_m$ is the output label score for voxel $\mathbf{x}_m \in \mathcal{X}'$, and $\mathcal{M}(\mathbf{x}_n^{\text{pt}}, \mathcal{X}')$ contains the coordinates of a set of voxels that the point \mathbf{x}_n^{pt} possibly exists after one attack step. Therefore, we can conduct the attack point-to-point in an end-to-end way as shown in (11).

Other details. For the layers other than sparse convolution, including linear layer, non-linear layer, normalization layer, and pooling layer, we also consider their existence that conditions on each voxel and multiply their outputs

Table 7. The class-specific semantic IoUs (%) on the S3DIS area 5 in budget $\epsilon = 0.01$ m.

Method	Clutter	Beam	Board	Bookcase	Ceiling	Chair	Column	Door	Floor	Sofa	Table	Wall	Window	Mean
Bf. Attack	52.9	0.1	68.6	67.1	91.9	87.6	37.3	72.7	96.7	55.7	72.8	82.6	51.8	66.4
Random	49.8	0.0	55.6	65.7	91.1	79.9	36.3	51.0	93.7	45.9	69.5	74.8	47.2	58.5
FGM	44.1	0.0	43.2	59.7	89.4	77.6	27.7	45.2	92.0	34.9	65.0	66.6	35.3	52.4
LGM	31.2	0.0	21.5	43.3	86.1	71.3	10.7	31.9	88.4	16.1	52.6	51.2	11.2	39.7

Table 8. The class-specific semantic IoUs (%) on the SemanticKITTI validation set in budget $\epsilon = 0.02$ m.

Method	Car	Bic.	Mot.	Truck	Bus	Pers.	Biclt.	Motlt.	Road	Park.	Sidew.	Other.	Build.	Fence	Vege.	Trunk	Teran.	Pole	Traffic.	Mean
Bf. Attack	97.1	54.5	80.9	85.1	70.3	76.5	92.2	0.0	94.6	44.8	81.2	1.0	90.5	58.7	86.6	70.8	70.5	64.2	51.8	66.9
Random	95.3	41.0	73.2	47.9	43.7	54.2	63.6	0.0	51.6	21.0	28.8	1.1	88.6	54.6	82.8	65.8	41.9	56.0	47.8	55.5
FGM	83.0	27.6	30.3	3.4	7.4	24.6	28.1	0.0	5.5	1.7	6.0	0.1	60.4	7.7	65.6	45.8	18.5	37.3	33.7	25.6
LGM	75.4	16.5	10.6	3.7	4.4	20.7	13.7	0.0	8.5	2.8	6.4	0.1	52.9	6.2	58.1	33.6	14.1	25.4	25.6	19.9

with occupancy values. If the stride $s > 1$, the output of the operation on each voxel is multiplied with a new occupancy value gathered with $g(\cdot)$ in (10) from a set of occupancy values covered by the stride space on the last layer.

C. More Experiment Results

In Table 7 and 8, we show the class-specific semantic IoUs on the S3DIS and SemanticKITTI datasets. We find *ceiling*, *chair*, *floor*, *table*, and *wall* are difficult to attack on the S3DIS dataset. These classes are consistent with the robust classes on the ScanNet dataset. For outdoor scene, we find *car*, *building*, *vegetation* are robust.